

THE ASTROSPHERE OF THE ASYMPTOTIC GIANT BRANCH STAR CIT 6

Raghvendra Sahai

*Jet Propulsion Laboratory, MS 183-900, California Institute of Technology, Pasadena, CA
91109*

sahai@jpl.nasa.gov

and

Galen P. Mack-Crane

Department of Physics, Occidental College, Los Angeles, CA 90041

ABSTRACT

We have discovered two extended half-ring structures in a far-ultraviolet image taken with the GALEX satellite of the well-known mass-losing carbon star CIT 6 (RW LMi). The northern (southern) ring is brighter (fainter) with a diameter of $\sim 15'$ ($\sim 18'$). These structures most likely represent the astrosphere resulting from the shock interaction of CIT 6's molecular wind with the Warm Interstellar Medium, as it moves through the latter. These data provide a direct estimate of the size of CIT 6's circumstellar envelope that is a factor ~ 20 larger than previous estimates based on CO millimeter-wave line data. We find that CIT 6 has been undergoing heavy mass-loss for at least 93,000 yr and the total envelope mass is $0.29 M_{\odot}$ or larger, assuming a constant mass-loss rate of $3.2 \times 10^{-6} M_{\odot} \text{ yr}^{-1}$. Assuming that the shock front has reached a steady-state and CIT 6's motion relative to the ISM is in the sky-plane, we measure the termination-shock standoff distance directly from the image and find that CIT 6 is moving at a speed of about $\gtrsim 39 (0.17 \text{ cm}^{-3}/n_{\text{ISM}})^{1/2} \text{ km s}^{-1}$ through the interstellar medium around it. However, comparisons with published numerical simulations and analytical modelling shows that CIT 6's forward shock (the northern ring) departs from the parabolic shape expected in steady-state. We discuss several possible explanations for this departure.

Subject headings: stars: AGB and post-AGB, stars: mass-loss, stars: individual (CIT 6), circumstellar matter, reflection nebulae

1. Introduction

The carbon-rich AGB star CIT 6 (RWLMi) is probably the most well-studied carbon star after IRC+10216 that is known to be experiencing heavy mass-loss during its Asymptotic Giant Branch (AGB) evolution. Such stars eject large quantities of processed material, enriched with carbon manufactured in their interiors as a result of $3\text{-}\alpha$ nucleosynthesis, into the interstellar medium via extensive dusty molecular winds that operate during the AGB phase. At 400 pc, CIT 6 is somewhat more distant than IRC+10216, and has been extensively observed from radio to optical wavelengths, with a variety of imaging and spectroscopic techniques.

The central star is a long-period variable with a period of about 640 days (Alksnis 1995), a bolometric luminosity of about $10^4 L_{\odot}$, and an average mass-loss rate of $3.2 \times 10^{-6} M_{\odot} \text{ yr}^{-1}$ (Zhang et al. 2009) resulting in a large circumstellar envelope (CSE) expanding at about 18 km s^{-1} . HST imaging at optical and near-infrared wavelengths reveals the presence of a small, roughly bipolar nebula, suggesting that the object is transitioning into the pre-planetary nebula phase (Schmidt et al. 2002). These authors also found the presence of faint, diffuse arcs $1'' - 4''$ from the central star, and suggested that the primary star has a main-sequence companion of spectral type A-F at a separation greater than 40 AU. Recently, Claussen et al. (2011) discovered the presence of multiple, partial circumstellar ring structures in CIT 6 at even larger distances from the center (up to $\sim 8''$), from their mapping of $\text{HC}_3\text{N J=4-3}$ emission using the VLA. These arc structures have been interpreted and modeled as a 3-dimensional spiral-shock structure induced in the CSE due to the presence of a binary companion (Kim et al. 2013).

The full extent of CIT 6's CSE has been traced most sensitively in CO J=1-0 emission, and has a half-power diameter of $35''$ (Neri et al. 1998). But since the outer extent of CO emission is limited by the photodissociation of this species by the interstellar ultraviolet radiation to $\sim 2 \times 10^{17} \text{ cm}$, direct evidence for AGB mass-loss in CIT 6 is limited to a relatively short (expansion) time-scale of about $\sim 3500 \text{ yr}$. Thus the total amount of matter

ejected into the ISM by CIT 6, which depends linearly on the envelope’s outer extent if the mass-loss has been constant, remains unknown, and likely vastly underestimated.

In this paper, we report deep GALEX images that trace the CIT 6 CSE to an outer radius that is more than an order of magnitude larger than the above estimate, and likely represents the full duration of the current heavy mass-loss. The outer edge of the CSE has become visible as a result of its interaction with the ISM as CIT 6 moves through the latter. We report our analysis of the shape, size and structure of the CSE-ISM interaction, and compare our results to those expected from theoretical models and numerical simulations. We determine CIT 6’s motion relative to the local ISM and provide new lower limits for the duration of heavy mass-loss and the total mass of ejecta in this object.

2. Observations & Results

We retrieved pipeline-calibrated FUV and NUV images of CIT 6 from the GALEX archive; the bandpass (angular resolution) is 1344-1786 Å(4.5”) and 1771-2831 Å(6.0”), respectively, and the pixel size is 1.5” × 1.5” (Morrissey et al. 2005). The data were taken on 2009 Feb 01, each with an exposure time of 30824 sec. In Fig. 1a, we show an FUV image of the star and its CSE, and in Fig. 1b, the corresponding NUV image. Field stars in the FUV image have been removed using a customised IDL routine which replaces a small region covering each star’s PSF with a tile of random noise representative of the surrounding sky. The sky noise was sampled separately at the four corners of each tile and linearly interpolated throughout, so as to preserve gradients in the local sky background to first order.

A magnified view of the relatively bright FUV nebula seen around CIT 6 is shown in Fig. 2. Bright nebulosity can be seen in the center of the FUV image, around the location of CIT 6’s central star. In addition, the image shows two bright, extended (size ~ 14’) half-ring structures, with diameters of about 15’ and 18’. No detectable counterpart to these ring structures is found in the NUV image (Fig. 1b).

Although the northern ring appears to be roughly circular around the central star’s location, closer inspection supported by examination of radial intensity cuts at different position angles (Fig. 3) shows it be flattened in the northerly direction. On the southern

side, the ring is not as prominently limb-brightened as in the north, mostly appearing as a bright edge which is roughly circular but at a larger radius from the central star than the northern ring (Fig. 4).

3. An Astrosphere around CIT 6

In a large imaging survey at 70 and 160 μm with the Herschel Space Observatory that revealed bow shocks for $\sim 40\%$, and detached rings for $\sim 20\%$, of a sample of 78 evolved stars (AGB stars and red supergiants), Cox et al. (2012: hereafter Cetal12) did not find any wind-ISM interaction structure around CIT 6. However, they did find “eye” shaped wind-ISM interaction structures (“two elliptical non-concentric arcs at opposing sides of the central source, both have a covering angle of $\lesssim 180^\circ$ ”) around seven AGB stars that resemble the northern and southern FUV ring structures in CIT 6. Given the strong indirect evidence that CIT 6’s central star is a binary, it is interesting that Cetal12 find that 5 of their 7 “eye” objects show evidence of binarity¹. Cetal12 stated that their data were not adequate to either confirm or exclude a connection between binarity and the “eyes” morphology. With the inclusion of CIT 6 to this list, the evidence for such a connection is strengthened.

A plausible interpretation of the FUV emission ring structures is that they represent the interaction of the expanding CSE of CIT 6 with the local ISM. We consider alternative interpretations later, but find them less likely (§ 6). The shorter radial distance and greater brightness of the northern ring from the star, compared to that of the southern one, implies that the star is moving roughly northwards through the local ISM, producing a strong shock front at the northern outer edge of its CSE.

The northern FUV ring around CIT 6 thus represents the astrosheath with the outer edge of this ring corresponding to the astropause, and the inner edge to the termination shock (see Fig. 2d, Ueta 2008). The region interior to the latter consists of the unshocked, freely-streaming stellar wind; the innermost part of this region is seen due to the scattering of ambient Galactic starlight from dust in the wind.

¹these 5 include 2 potential binaries and 3 visual binaries: see Cetal12’s Table 1 for details and references

A similar large astrosphere was found around IRC+10216 in GALEX images by Sahai & Chronopoulos (2010: SC10). Assuming, as for IRC+10216’s astrosheath (SC10), that the FUV emission mechanism is due to collisional excitation of H₂ by hot electrons in shocked gas, which produces no detectable counterpart in the NUV band (see Martin et al. 2007), the non-detection of the ring structure in the NUV is not surprising. We note that the brightest region of the astrosheath has an excess FUV intensity (over the background) of about 0.013 $\mu\text{Jy pix}^{-1}$, whereas the 3σ noise in the NUV in this region is 0.036 $\mu\text{Jy pix}^{-1}$. Assuming the relative FUV-to-NUV brightness for the astrosheath in CIT 6 is the same as in IRC+10216 (about 6, SC10), the CIT 6 NUV image, even with smoothing to reduce the noise, lacks the sensitivity needed to detect a counterpart to the FUV emission

We follow a similar procedure as described in SC10 to analyze CIT 6’s astrosphere. We measured the northern ring’s radial offset in different directions from the central star, using radial intensity cuts at different position angles. Since the emission from the ring (the astrosheath) is rather faint, we averaged the intensity over seven 23° wedges spanning the northern limb. These cuts (Fig. 3) show that the radius of the astrosheath varies systematically, reaching a minimum roughly in the northward direction, and implying that CIT 6 motion through the local ISM is indeed northward.

We have fit a model radial intensity curve derived from a limb-brightened spherical shell to the FUV radial brightness profiles, assuming the surface brightness to be proportional to the column density, and extracted the astrosheath’s inner and outer radii (R_1 and R_c , using the nomenclature in Fig. 1 of Weaver et al. 1977). We assumed a two-piece inverse-square density profile in our model, one for $120'' \lesssim r < R_1$, and the other for $R_c > r > R_1$, with a jump in density at $r = R_1$.

From a 46° wedge centered at $PA = 2^\circ$ which encloses the symmetry axis (Fig. 5a), we find $R_1 = 373''$ and $R_c = 396''$. These values of R_1 and R_c are not sensitive to the assumed density profiles within these two regions, as they are largely determined by the radial location of the intensity peak and the radial width of the steeply-falling intensity curve just beyond this peak (e.g., see model fit in Fig. 5a).

We cannot derive absolute values of the densities from our modelling since the proportionality factor between the brightness and the column density is purely phenomenological;

furthermore, since the emission mechanisms in the two regions are different, the value of the derived density jump is not physical.

We note the systematic presence of a “shoulder” in the FUV radial intensity cuts, extending to about $50''$ beyond the outer edge of the astropause ($r = R_c$) in the four cuts nearest to the symmetry axis. Although comparably bright features are also seen at larger radii beyond this shoulder, their location varies from cut to cut. It is plausible that these features have the same origin as other patchy emission regions that are present in many other parts of the full field-of-view (see Fig. 1a), and are likely due to scattered light from dust in the ISM, unrelated to CIT 6. Our tentative conclusion is that the shoulder emission is due to a coherent structure that lies just outside the astropause, i.e., $r > R_c$ – this structure can be seen marginally in Fig. 5b, and probably represents the bow-shock interface separating the shocked and unshocked ISM. A similar structure was found by SC10 in IRC+10216.

The post-shock temperature in the bow-shock region is expected to be high, about $(3/16k) \bar{\mu} V_*^2 \sim 2 \times 10^4 \text{K}$ (assuming a strong shock, where the stellar velocity relative to the ISM, $V_* = 39 \text{ km s}^{-1}$, § 4), where $\bar{\mu} \sim 10^{-24} \text{ g}$ is the mean mass per particle for fully ionized gas. The emission in this region is thus most likely dominated by the two-photon continuous emission of H (Spitzer & Greenstein 1951).

4. CIT 6’s Motion through the ISM, Mass-Loss Duration and Circumstellar Mass

We estimate the star’s velocity V_* through the surrounding ISM using the relationship between l_1 , the distance of the termination shock from the star along the astropause’s symmetry axis (i.e., the termination-shock standoff distance), and $V_*(\text{km s}^{-1}) = 10 V_{*,6}$ (Eqn. 1 of van Buren & McCray 1988²):

$$l_1(\text{cm}) = 1.74 \times 10^{19} (\dot{M}_{*,-6} V_{w,8})^{1/2} (\bar{\mu}_H n_{\text{ISM}})^{-1/2} V_{*,6}^{-1} \quad (1)$$

where $\dot{M}_{*,-6}$ is the stellar mass-loss rate in units of $10^{-6} M_\odot \text{ yr}^{-1}$, $V_{w,8}$ is the wind velocity

²there is a missing minus sign in the exponent of $\bar{\mu}_H$ in their equation, which we have corrected below

in units of 10^3 km s^{-1} , $\bar{\mu}_H$ is the dimensionless mean molecular mass per H atom, and n_{ISM} is the ISM number density in cm^{-3} .

Given the strong asymmetry between the northern and southern hemispheres, we first make the simplifying assumption that the astropause’s symmetry axis lies in the sky-plane, i.e., the inclination angle, $\phi = 90^\circ$. We find $l_1 = R_1 D = 2.2 \times 10^{18} \text{ cm}$, using the value of $R_1 = 373''$ derived earlier, and the distance $D=400 \text{ pc}$. Substituting this value of l_1 in Eqn. 1, with $\dot{M}_{*,-6} = 3.2$, $V_{w,8} = 0.018$, and $\bar{\mu}_H = 1.33$ (for an 89/11 mixture of H/He), we find $V_* = 39 (n_{\text{ISM}}/0.17)^{-1/2} \text{ km s}^{-1}$. Our choice of n_{ISM} is discussed in § 4.1. The value of V_* (i) does not depend on the (uncertain) distance, D , to CIT 6, since both l_1 and $\dot{M}_{*,-6}^{1/2}$ scale linearly with D , and (ii) depends only weakly on the uncertain value of the ISM density at CIT 6’s location. The inclination angle ϕ may be significantly smaller than 90° – we discuss this in § 4.3.

4.1. Density of the ISM around CIT 6

We estimate the ISM number density near CIT 6 based on the star’s location in the Galaxy as follows. First we determine the the density of neutral hydrogen, HI around CIT 6. We approximate the HI disk scale height $h_z(R)$ using the relation (Kalberla & Kerp 2009)

$$h_z(R) = h_0 e^{(R-R_\odot)/R_0}, \text{ for } 5 < R < 35 \text{ kpc}, \quad (2)$$

where R is the Galactocentric radius, and R_\odot is the distance of the Sun from the Galactic center, and $h_0 = 0.15 \text{ kpc}$, $R_0 = 9.8 \text{ kpc}$. Taking $R_\odot = 8.33 \text{ kpc}$ (Gillessen et al 2009), and using CIT 6’s galactic coordinates ($l = 197^\circ.7147$, $b = +55^\circ.9642$, its distance from the Sun of 0.4 kpc , we find $R = 8.44 \text{ kpc}$, which implies $h_z(8.44) = 0.152 \text{ kpc}$. The midplane density of HI (i.e., at $z = 0$) is found from the relation (Kalberla & Kerp 2009)

$$n_{\text{HI}} \sim n_0 e^{-(R-R_\odot)/R_n} \text{ for } 7 < R < 35 \text{ kpc}, \quad (3)$$

where $n_0 = 0.9 \text{ cm}^{-3}$ is the density at $R = 0$ and $R_n = 3.15 \text{ kpc}$. Combining the midplane HI density at CIT 6’s Galactocentric radius, $n_{\text{HI}} \sim 0.87$, with the fractional HI density of 0.038 (given by $e^{-\ln(2)(z/h_z)^2}$) at CIT 6’s height above the galactic plane ($z = 0.33 \text{ kpc}$),

we find a relatively low value for the HI density, $n_{\text{HI}} \sim 0.033$. Thus it is likely that the ISM surrounding CIT 6 is ionized and that CIT 6 is embedded in the Warm Ionized Medium (WIM), specifically its thick-disk that extends more than a kpc above and below the Galactic plane. The volume-filling factor of the WIM in the midplane in this region is $f = 0.04 \pm 0.01$, which grows exponentially with z over the $0 - 1.4$ kpc range as $e^{|z|/H_f}$, where the scale height $H_f \sim 0.7$ kpc. (Gaensler et al. 2008). In the neighborhood of CIT 6, $f(z = 0.33 \text{ kpc}) = 0.065$. Because the volume-filling factor is small, n_{ISM} is likely less than n_{typ} , where n_{typ} is the typical internal electron density for clouds in the thick-disk component of the WIM. In the midplane, $n_{\text{typ}} = 0.34 \pm 0.06 \text{ cm}^{-3}$ and decays with z as $e^{-|z|/H_N}$, where the scale height $H_N = 0.5$ kpc (Gaensler et al. 2008).

In the neighborhood of CIT 6, $n_{\text{typ}}(z = 0.33 \text{ kpc}) = 0.17 \text{ cm}^{-3}$. Assuming that CIT 6 is embedded in a WIM cloud, $n_{\text{ISM}} = 0.17 \text{ cm}^{-3}$, which is the value that we use for our estimate of V_* . Our value of n_{ISM} is larger than an estimate by Cetal12, who find $n_{\text{ISM}} \approx 0.04 \text{ cm}^{-3}$, assuming a representative global average of the density given by $n_H(z) = 2e^{(-|z|/100\text{pc})}$, although acknowledging that the structure of the ISM entails fluctuations in the density (and filling factor) on all spatial scales.

4.2. Duration of Mass Loss and Circumstellar Mass

The FUV emission traces the AGB stellar wind in CIT 6 to a much larger distance from the star than that derived from previous measurements of the CO J=1-0 and 2-1 emission (Neri et al. 1998). These authors take the CSE outer radius to be that at which CO is photodissociated by the interstellar radiation field. Since the photodissociation radius depends on $\dot{M}^{0.58}$ and Neri et al. (1998) use $\dot{M}=7.2 \times 10^{-6} M_{\odot} \text{ yr}^{-1}$, we scale their value of this radius for our mass-loss rate $\dot{M}=3.2 \times 10^{-6} M_{\odot} \text{ yr}^{-1}$ to derive a photodissociation radius of $1.7 \times 10^{17} \text{ cm}$. This estimate of the CSE outer radius implies a mass-loss duration of 3500 yr.

We use the astropause size to substantially revise (upwards) the above estimate of the duration, P , of heavy mass-loss in CIT 6. We take the radius of the termination shock in the direction orthogonal to the symmetry axis ($432''$ or $2.6 \times 10^{18} \text{ cm}$ at $D = 400 \text{ pc}$) as a measure of the outer radius to which the unshocked wind has expanded, since the radial

extent in that direction is independent of the inclination angle.

We estimate P by deriving expansion time-scales (P_u, P_s) for the unshocked and shocked wind regions separately; $P_u = 45,240$ yr from the ratio of the termination shock radius to V_w , and $P_s = 47,950$ yr from the ratio of the astrosheath width ($38''$) to an average velocity for this region, $\bar{V}_s = 1.50 \text{ km s}^{-1}$. We take $\bar{V}_s = V_s/2$, where $V_s = V_w (\gamma - 1)/(\gamma + 1) = V_w/6 = 3.00 \text{ km s}^{-1}$, is the velocity in the astrosheath just beyond the termination shock, with $\gamma = 7/5$ for diatomic gas, and assuming the latter to be adiabatic. The actual value of V_s should be less than the adiabatic value, since the astrosheath appears to have cooled to some degree – the astrosheath’s width of $38''$, or 2.3×10^{17} cm, derived from fitting the radial intensity cut in a direction orthogonal to the symmetry axis, is smaller than the adiabatic value, $\approx 0.47 l_1 = 1.0 \times 10^{18}$ cm (Eqn. 2, Van Buren & McCray 1988) by factor of about 4. Furthermore, once a complete balance has been established between the ram pressure of the stellar wind and that of the ISM, the leading edge of the astropause (i.e., the forward shock structure) remains a fixed distance ahead of the moving star (Weaver et al. 1977). Hence, if the shock interaction of CIT 6’s wind with the ISM has reached equilibrium, $P = P_u + P_s = 93,190$ yr is a lower limit, in which case CIT 6 has been undergoing mass-loss for at least 93,000 years, and the total CSE mass is $> 0.29 M_\odot$.

Model fits to IRAS far-infrared scan data have been used to derive dust shell sizes for a large sample of AGB stars, including CIT 6 by Young et al. (1995: Yetal95) – for the latter, they estimated an outer radius of $7'$. However, this result must be regarded with caution as (a) inspection of the data and model fits by Yetal95 for CIT 6 (see their Fig 7, panels D(i) and D(ii)), as well as many other stars in their sample, shows the presence of large negative and positive fluctuations in the derived intensity profile of the extended dust-shell emission, (b) the Herschel PACS imaging data in the Cetal12 study did not reveal an extended dust shell around CIT 6, and (c) a comparison of the outer radii of the dust shells for a sample of AGB stars in Yetal95 with those reported to have bow-shock (Class I), eye (Class II), or ring (Class III) structures in Cetal12, shows that the IRAS-based value is significantly larger (i.e., by factors as large as $\sim 2 - 5$).

It is possible that the shells inferred from the IRAS data represent circumstellar structures that lie beyond the dust structures found with Herschel, but were not detected by the latter because of inadequate sensitivity. For example, in the case of Y CVn, an extended dust

shell is clearly seen in ISO maps (Izumiura et al. 1996) with about the same size as inferred by Yetal95, but only very faintly in the Cetal12 study. However, for CRL2688, where Speck et al. (2000) reported the presence of two dust shells from ISO scan data, Spitzer imaging by Do et al. (2007) showed no such shells at a level well below the intensities expected from the ISO results. We believe that a detailed re-investigation is needed to resolve such discrepancies in results related to the presence of extended dust shells as derived from IRAS and ISO, and from the more recent Spitzer and Herschel missions (utilizing modern large-format detector arrays).

If, however, the much larger circumstellar shells inferred by Yetal95 are real, then their presence poses a problem for each such object common to the Cetal12 study in which the (smaller) dust shell represents a bow-shock structure due to the wind-ISM interaction resulting from the object’s motion through the ISM (based on its morphology, i.e., Class I and possibly Class II). In order to resolve this problem, one would require the ISM to be streaming through “holes” in the outer IRAS-detected shell in order to interact with the inner circumstellar shell in these objects – numerical simulations would be needed to determine if this is a plausible scenario.

4.3. Forward Shock Shape and Inclination

Has CIT 6’s forward shock structure reached a steady state? The shape of this structure is expected to change with time, being initially circular and becoming increasingly parabolic until it reaches its steady state morphology (Weaver et al. 1977), given by the analytic solution of Wilkin (1996). We define $\eta(0/90)$ as the ratio between the radius of the termination shock along the shock’s symmetry axis to that along an orthogonal direction. Employing Eqn. 9 in Wilkin (1996), the analytic value is $\eta(0/90) = 1/3^{1/2} = 0.577$, and is reached after $\sim 40,000$ yr in simulations of astrospheres around AGB stars that are applicable to CIT 6 (see Fig. 11 of Mohamed et al. 2012 [MML12]). However, from CIT 6’s observed shock structure, we find $\eta(0/90) = 373/432 = 0.86$, assuming that the inclination angle is, $\phi = 90^\circ$.

The discrepancy between the observed and expected steady-state value of $\eta(0/90)$ in CIT 6 is not unprecedented – a similar discrepancy exists for the forward shock structures seen in IRC+10216 and the red supergiant Betelgeuse, where this parameter is ~ 0.8 (SC10,

Decin et al. 2012).

In the MML12 simulations, $\eta = 0.86$ corresponds to an age of only $\sim 5,000$ years. We found earlier that CIT 6 has been undergoing mass loss for a period at least as long as $P_u = 45,240$ yr, and possibly much longer. If it has been interacting with the ISM during most of this period it is likely to have reached a steady state, in which case the discrepancy between the observed and expected values of $\eta(0/90)$ would imply that the star’s direction of motion of the star is not in the plane of the sky.

Mac Low et al.’s (1991: MLetal91) paraboloidal shock models for various inclination angles (their Fig. 5) show that as ϕ becomes *smaller*, the ratio of the radial distance between the star and the apex of the projected emission paraboloid, to the (unprojected) standoff distance, becomes *larger*. A visual comparison of CIT 6’s FUV emission morphology (Fig. 1) with the surface brightness contours in Fig. 5 of MLetal91, indicate that ϕ is small, $\sim 30^\circ$, and our measured value of R_1 is larger than l_1 by a significant factor. We estimate that this factor may be as large as $\sim 1.5 - 2$, by comparing the length of the unprojected standoff distance vector, to its apparent value as estimated from the distance between the star and the apex defined by the emission contours for $\phi = 30^\circ$ and 90° in Fig. 5 of MLetal91. Thus the value of V_* may be as high as $\sim 70 \text{ km s}^{-1}$.

The value of ϕ depends on the orientation of the relative motion vector between CIT 6 and the WIM cloud with which it is interacting. Thus, if both CIT 6 and the WIM cloud have similar radial velocities, then the relative motion vector would lie in the sky plane, i.e., $\phi \sim 90^\circ$. CIT 6’s radial velocity is $V_{lsr} = -1.5 \text{ km s}^{-1}$ (Olofsson et al. 1993). For the WIM, Haffner et al. (2003) conclude, using data from the Wisconsin H α (WHAM) survey that the H α emitting gas at high galactic latitudes is clearly biased towards negative V_{lsr} values; inspection of the longitude-velocity plots for $b=50^\circ$ and 60° in Fig. 9 of their paper shows relatively strong emission extending to V_{lsr} values of -50 to -75 km s^{-1} at CIT 6’s longitude. Thus, it is quite possible that the relative motion vector between CIT 6 and the local WIM has a significant radial component, implying that ϕ is significantly less than 90° .

Alternatively, the density of the ISM around CIT 6 is much lower than $few \times 0.1 \text{ cm}^{-3}$, or its mass-loss rate was significantly higher in the distant past (since the time required to reach a steady state varies as $(n_{ISM}/\dot{M})^{1/2}$, Weaver et al. 1977). It is also possible

that CIT 6 has only recently entered the higher-density region with which it is interacting – this alternative finds some support in the relatively smooth shock structure observed in CIT 6, as hydrodynamical instabilities take time to develop. For example, MML12 attribute the smoothness of the shock structure of Betelgeuse to the bow-shock interaction being too young for instabilities to have developed (they constrain the age to $< 30,000$ yr). A note of caution here is in order – the production of instabilities in different simulation studies varies significantly, both in terms of the time-scales over which they are produced and in their size and structure, as noted by Decin et al (2012) while comparing their simulations of the bow-shock around the red supergiant Betelgeuse with those of MML12 and Cetal12.

Other explanations for a smooth shock structure are also possible, including the suppression of large scale instabilities due to a warm ISM (Decin et al 2012) (which may be appropriate for CIT 6), and the presence of a magnetic field in the direction of motion (van Marle et al. 2014).

4.4. Comparison with IRC+10216

It is instructive to compare the astrosphere of CIT 6 with that of IRC+10216, the only other carbon-rich star that has been found to show such a structure in GALEX images (SC10). SC10 noted that IRC+10216’s forward shock structure is relatively smooth and does not show the large-scale instabilities expected in such interactions (Blondin & Koerwer 1998), and CIT 6 is similar in this respect. While the absence of large-scale instabilities for CIT 6’s shock may be explained as a result of it being surrounded by a warm ISM, this explanation is not applicable for IRC+10216, which (as we show below) is most likely immersed in neutral (and cooler) gas.

Given IRC+10216’s Galactocentric radius $R = 8.36$ kpc (derived from its galactic coordinates $l = 221^\circ.4466$, $b = +45^\circ.0604$, and $D=120$ pc), we find the HI scale height to be $h_z = 0.15$ kpc, giving a fractional density of 0.80 at its height above the Galactic plane of $z = 85$ pc. With a mid-plane density of 0.89 cm^{-3} at $R = 8.36$ kpc, the density of HI near IRC+10216 is then $\sim 0.72 \text{ cm}^{-3}$, implying that the ISM near IRC+10216 is probably largely neutral (supporting SC10’s choice of $n_{\text{ISM}} = 1 \text{ cm}^{-3}$), thus significantly cooler than the WIM.

The morphologies of the astrotail regions of CIT 6 and IRC+10216 differ markedly, with CIT 6 showing a relatively smooth arc structure, whereas IRC+10216 shows prominent vortices. SC10 attribute these as resulting from the vortex shedding seen in numerical simulations of AGB wind-ISM interactions that occurs at very long interaction time-scales ($\sim 500,000$ yr) (Wareing et al. 2007). Thus it appears that the period of wind-ISM interaction in IRC+10216 is much longer than that of CIT 6.

5. Comparison with 3D Numerical Simulations

We compare our observations of CIT 6 with the results of 3D simulations of the bow-shock around Betelgeuse (α Ori) by MML12, since there is reasonable similarity between the physical parameters relevant to the shock structure employed in these models and those applicable to CIT 6. MML12’s model D has $\dot{M}_* = 3.1 \times 10^{-6} M_\odot \text{ yr}^{-1}$, $V_w = 17 \text{ km s}^{-1}$, $V_* = 72.5 \text{ km s}^{-1}$ and $n_{\text{ISM}} = 0.3$. The density structure for model D (rightmost panel of Fig. 7 in MML12) appears quite similar to our image of CIT 6 – specifically, the density plot shows the presence of a high-density semi-circular structure in the direction of motion (leftwards in this figure), and a roughly semi-circular “edge” structure in the opposite direction. The latter is at a larger radial distance from the central star than the former, similar to what we observe in CIT 6, and shows a density contrast of a factor 10 or more relative to the immediate environment beyond it (seen in red/brown hues). We note that the parabolic-shaped structure seen in yellow in MML12’s Figure 7 represents high-temperature ($> 10^4$ K) ionized gas in the bow-shock, which at best is only seen very faintly, and only around the forward shock in our observations – hence its absence in the tail region of the observed astrosphere of CIT 6 is most likely due to inadequate sensitivity. The southern ring, like the northern one, is only seen in FUV emission and not in the NUV, suggesting that the emission mechanism for the former is the same as the latter, namely, collisional excitation of H_2 by hot electrons.

MML12 find that the gas in the “bow shock arc (where the gas is strongly decelerated)”, i.e., the astrosheath in our description, behaves nearly isothermally, consistent with our finding for CIT 6 that the average astrosheath width is significantly smaller than the expected adiabatic value (§4.2). But as noted earlier, in the simulation the stellar wind-ISM interaction

has been ongoing for 32,000 yr and is close to steady state with $\eta(0/90) \sim 0.6$, whereas the observed value of $\eta(0/90)$ is significantly higher.

6. Alternative Models for the FUV Rings around CIT 6

We now consider alternatives to the astrosphere model for the origin of the FUV emission rings around CIT 6. Given the presence of the partial arcs seen by Claussen et al. (2011) and Schmidt et al. (2002) within $\sim 8''$ of the central star, believed to be created by a spiral shock due to the presence of a central binary, one possibility is that the much more distant FUV emission rings also have the same origin. In this model, the radial pitch of the spiral, i.e., the separation between successive windings is equal to $P V_{exp}$, where P is the binary period and V_{exp} is the expansion velocity of the CSE (e.g., Mauron & Huggins 2006). Hence, assuming V_{exp} does not change substantially over the timescales corresponding to the rings, the current separation of the windings ($\sim 2''.6$), provides an upper limit to the separation in the past (because the period P of the binary increases as the central star loses mass via its wind). Clearly, given the much larger observed difference in the average radius of the northern and southern rings ($\sim 200''$), these cannot represent successive windings, even if we allowed for a V_{exp} that was larger in the past by a factor 10 over its current value.

Another possible model is one in which the northern and southern rings represent two discrete mass-loss episodes in CIT 6's distant past. However, such a model would then require that each of these episodic ejections was confined to only a hemispherical region – with either both ejections occurring at different times with roughly the same velocity, or at the same time with different velocities (or some combination of these). Such a mass-ejection history would be unprecedented for an AGB star, and would not fit into the standard model of roughly spherical AGB mass-loss (i.e., driven by radiation pressure on dust grains). It also does not provide an explanation for the systematic increase in the radius of the northern ring around its symmetry axis. We note that although the so-called detached shell phenomenon observed in a few carbon-rich stars does produce large single shell structures (e.g., the Class III objects in the Cet12 survey), these shells, believed to result from a relatively short episode of enhanced mass-loss rate (and possibly wind velocity as well) initiated by a He-shell flash (e.g., Olofsson et al. 1990, Steffen & Schönberner 2000), are circular and complete

and thus morphologically different from CIT 6’s FUV emission rings.

7. Concluding Remarks

In summary, the GALEX images of CIT 6 show an unusually detailed picture of the interaction of the wind from a carbon-rich AGB star with the ISM due to its motion in the latter. This interaction process has been studied using UV and far-infrared observations for other AGB stars (e.g., SC10, Cetal12 and references therein) and a red supergiant (α Ori: Ueta et al. 2008, Decin et al. 2012, le Bertre et al. 2012), as well as HI 21 cm line observations (Matthews et al. 2013, and references therein). The far-infrared imaging observations with Herschel by Cetal12 have discovered the largest number of astrospheres by far, clearly tracing the detailed geometry of the shock front in the wind-ISM interaction for a large sample of AGB stars. The HI observations reveal, for a smaller sample, that the CSEs have been significantly influenced by the wind-ISM interaction, but since the angular resolution of these observations is relatively low ($\sim 1'$), it is difficult to spatially separate the detailed shape and structure of the astropause from the HI emission of the CSE as a whole. However, kinematical information extracted from the observed HI line profiles provides support for deceleration of the freely expanding CSE by the ISM.

Including CIT 6, there are now three examples of AGB stars (IRC+10216, Mira, and CIT 6) and one RSG (α Ori) that show astrospheres in FUV emission. An exhaustive search of the GALEX image archive in order to determine if there are additional such examples would be useful, but is outside the scope of this paper. However, we speculate that such a search would not be very succesful given the very long exposure times that were needed for the GALEX imaging to reveal the relatively faint FUV emission from the wind-ISM interaction in these objects (e.g., 30,824 s for CIT 6; 8783 s for IRC+10216; 48,915 s for α Ori.)

Our study provides valuable new data for understanding the CSE-ISM interaction, and shows that there are specific features in the resulting shock structures that are not adequately reproduced by current numerical simulations. These features include the relatively high value of the parameter $\eta(0/90)$ compared to the steady-state value, and the relative smoothness of the shock structure implying the general lack of large-scale instabilities. Given that such discrepancies are seen in other objects as well, new modelling that is focussed on

addressing these will help improve our understanding of this interaction, and our ability to make inferences about the unprecedented long history of AGB mass-loss revealed by these interactions. For example, one avenue that merits detailed investigation is when the wind-ISM interaction involves an encounter of the star’s CSE with a relatively high density cloud in an inhomogeneous ISM, so that the timescale for the interaction is substantially smaller than the mass-ejection timescale.

We would like to thank an anonymous referee for detailed comments that have helped us improve the discussion in this paper. RS’s contribution to the research described in this publication was carried out at the Jet Propulsion Laboratory, California Institute of Technology, under a contract with NASA. RS thanks NASA for financial support via a GALEX GO and ADAP award. GMC thanks JPL for a NASA Student Independent Research Internship (SIRI).

REFERENCES

- Alksnis, A. 1995, *Baltic Astronomy*, 4, 79
- Blondin, J. M., & Koerwer, J. F. 1998, *New Astronomy*, 3, 571
- Claussen, M. J., Sjouwerman, L. O., Rupen, M. P., et al. 2011, *ApJ*, 739, L5
- Cox, N. L. J., Kerschbaum, F., van Marle, A.-J., et al. 2012, *A&A*, 537, A35
- Decin, L., Cox, N. L. J., Royer, P., et al. 2012, *A&A*, 548, A113
- Do, T., Morris, M., Sahai, R., & Stapelfeldt, K. 2007, *AJ*, 134, 1419
- Gaensler, B. M., Madsen, G. J., Chatterjee, S., & Mao, S. A. 2008, *PASA*, 25, 184
- Gillessen, S., Eisenhauer, F., Trippe, S., et al. 2009, *ApJ*, 692, 1075
- Haffner, L. M., Reynolds, R. J., Tufte, S. L., et al. 2003, *ApJS*, 149, 405
- Izumiura, H., Hashimoto, O., Kawara, K., Yamamura, I., & Waters, L. B. F. M. 1996, *A&A*, 315, L221

- Kalberla, P. M. W., & Kerp, J. 2009, *ARA&A*, 47, 27
- Kim, H., Hsieh, I.-T., Liu, S.-Y., & Taam, R. E. 2013, *ApJ*, 776, 86
- Le Bertre, T., Matthews, L. D., Gérard, E., & Libert, Y. 2012, *MNRAS*, 422, 3433
- Mac Low, M.-M., van Buren, D., Wood, D. O. S., & Churchwell, E. 1991, *ApJ*, 369, 395
- Martin, D. C., et al. 2007, *Nature*, 448, 780
- Matthews, L. D., Le Bertre, T., Gérard, E., & Johnson, M. C. 2013, *AJ*, 145, 97
- Mauron, N., & Huggins, P. J. 2006, *A&A*, 452, 257
- Mohamed, S., Mackey, J., & Langer, N. 2012, *A&A*, 541, A1
- Morrissey, P., et al. 2005, *ApJ*, 619, L7
- Neri, R., Kahane, C., Lucas, R., Bujarrabal, V., & Loup, C. 1998, *A&AS*, 130, 1
- Olofsson, H., Carlstrom, U., Eriksson, K., Gustafsson, B., & Willson, L. A. 1990, *A&A*, 230, L13
- Olofsson, H., Eriksson, K., Gustafsson, B., & Carlstrom, U. 1993, *ApJS*, 87, 267
- Sahai, R., & Chronopoulos, C. K. 2010, *ApJ*, 711, L53
- Schmidt, G. D., Hines, D. C., & Swift, S. 2002, *ApJ*, 576, 429
- Speck, A. K., Meixner, M., & Knapp, G. R. 2000, *ApJ*, 545, L145
- Spitzer, L., Jr., & Greenstein, J. L. 1951, *ApJ*, 114, 407
- Steffen, M., & Schönberner, D. 2000, *A&A*, 357, 180
- Ueta, T. 2008, *ApJ*, 687, L33
- Ueta, T., et al. 2008, *PASJ*, 60, 407
- van Buren, D., & McCray, R. 1988, *ApJ*, 329, L93
- van Marle, A. J., Decin, L., & Meliani, Z. 2014, *A&A*, 561, A152

Wareing, C. J., Zijlstra, A. A., & O’Brien, T. J. 2007, *ApJ*, 660, L129

Weaver, R., McCray, R., Castor, J., Shapiro, P., & Moore, R. 1977, *ApJ*, 218, 377

Wilkin, F. P. 1996, *ApJ*, 459, L31

Young, K., Phillips, T. G., & Knapp, G. R. 1993, *ApJS*, 86, 517

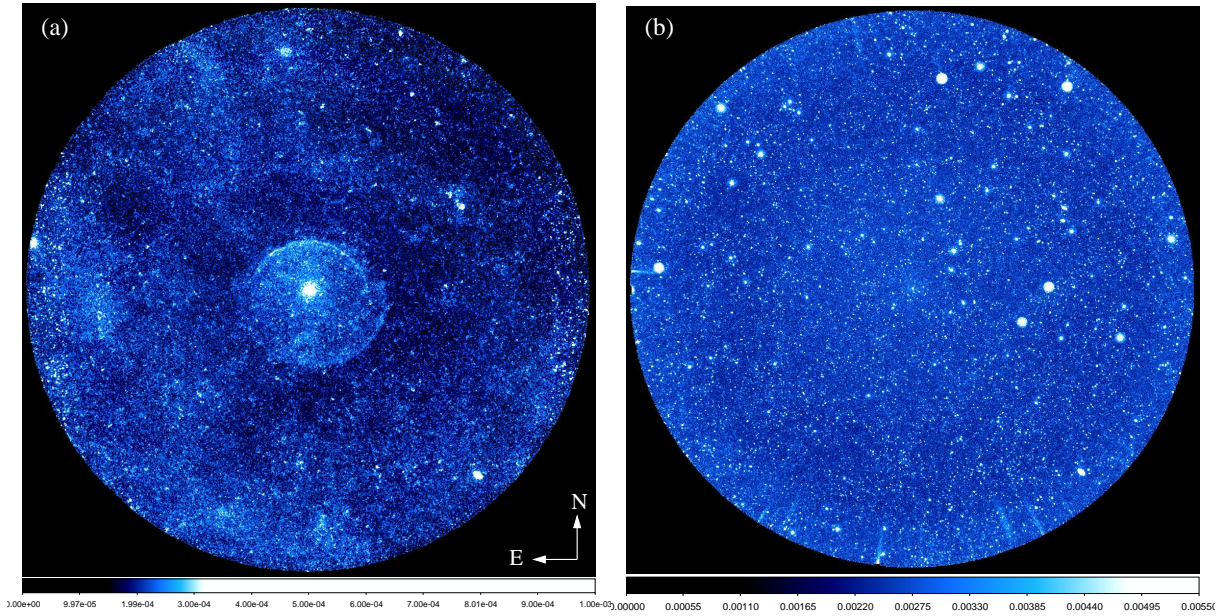


Fig. 1.— (a) FUV GALEX image of CIT 6 (the circular field-of-view (FOV) has a diameter of $72.8' \times 72.8'$); the image was boxcar-smoothed using a 3×3 pixel box, and displayed using a linear stretch (in false color). Units in the colorbar are cps/pixel, implying a flux of $107 \mu\text{Jy}$ per $1.5'' \times 1.5''$ pixel (b) NUV GALEX image of CIT 6 (same FOV as in a), displayed using a linear stretch (in false color). Units in the colorbar are cps/pixel, implying a flux of $35.3 \mu\text{Jy}$ per $1.5'' \times 1.5''$ pixel

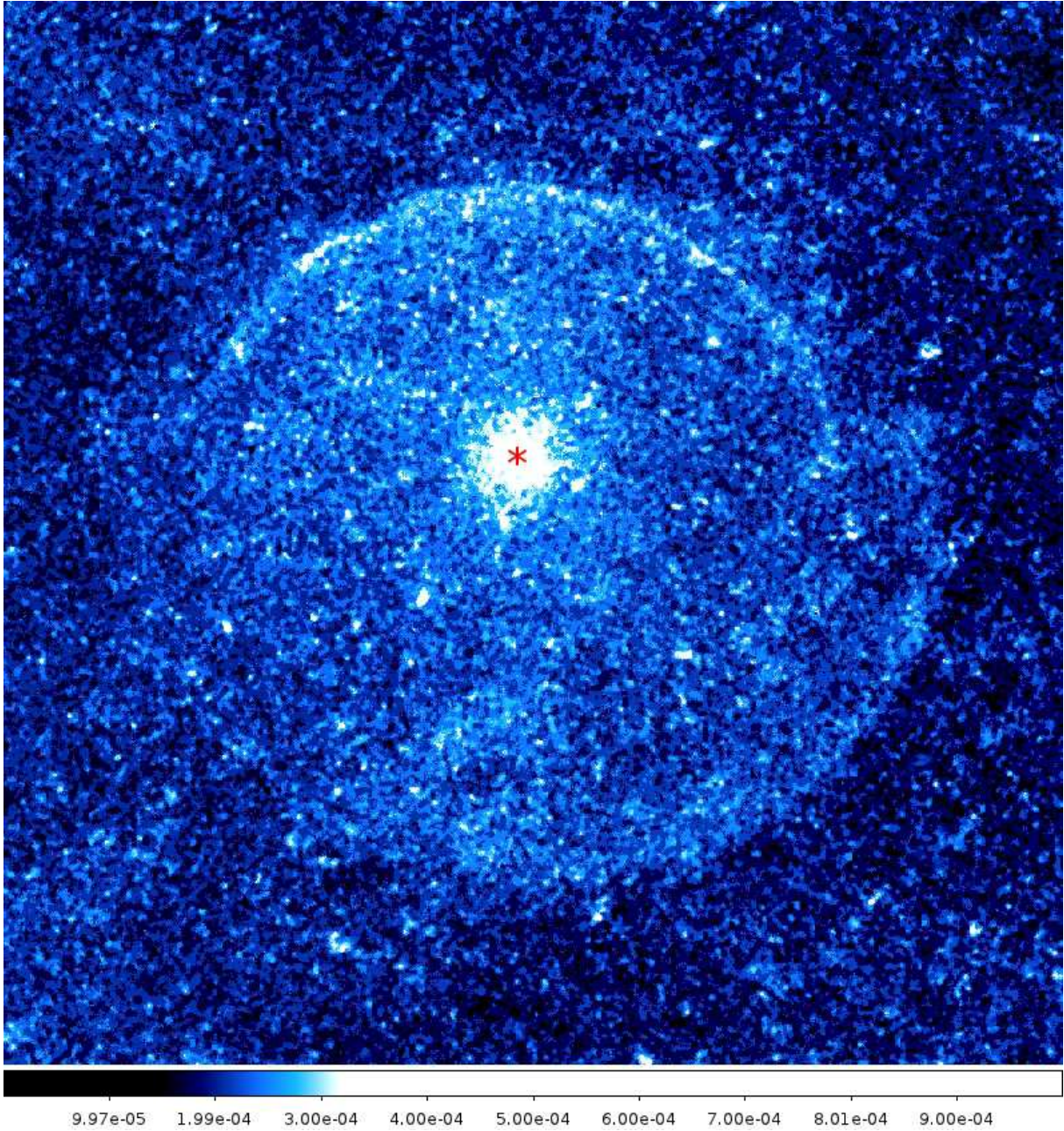


Fig. 2.— As in Fig. 1(a), but showing a magnified view of the FUV emission structures around CIT 6. The panel size is $24.75' \times 24.75'$. The location of the central star is marked with a *.

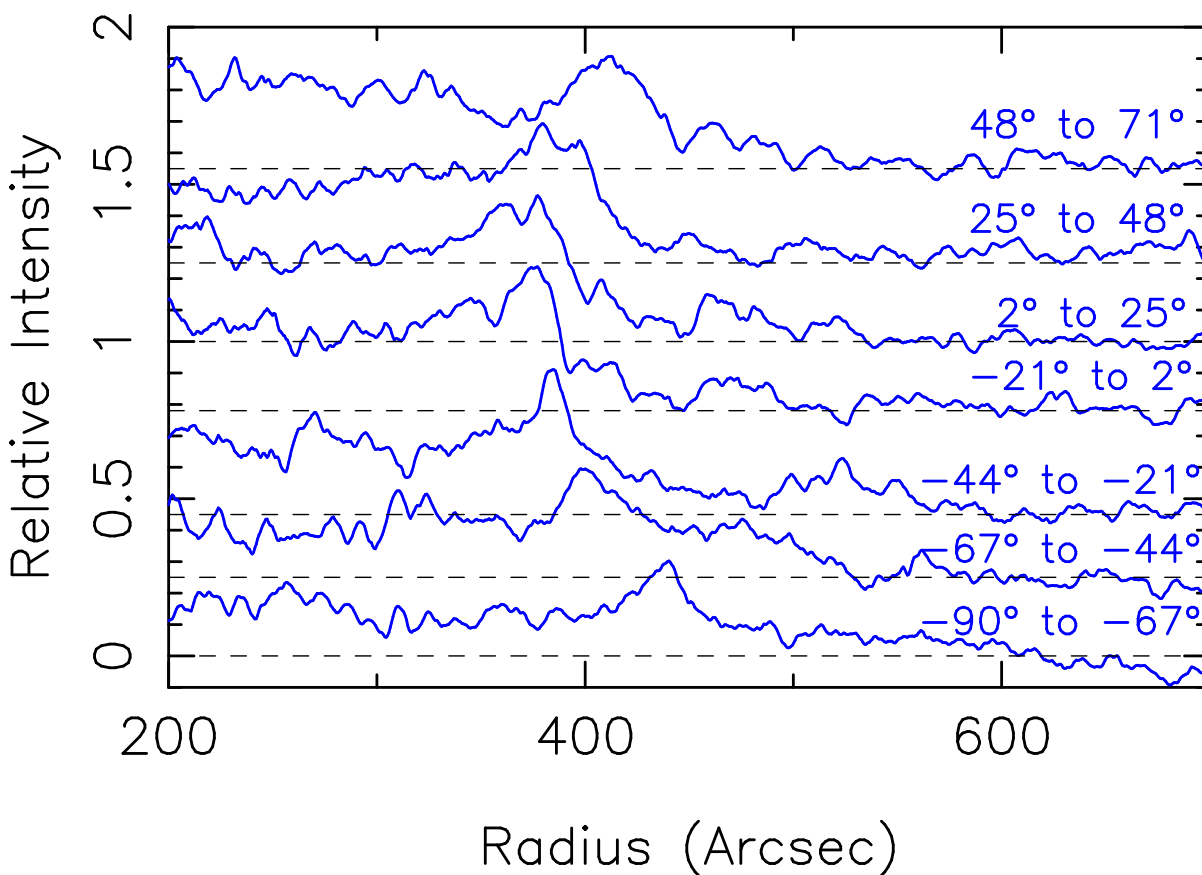


Fig. 3.— Cuts (solid blue curves) of the radial intensity averaged over each of seven 23° angular wedges spanning the northern ring seen in the FUV emission nebula around CIT 6. The intensity cuts have been shifted vertically by constant offsets, indicated by black dashed lines, for clarity. The cut PAs are noted above the cuts on the image. Intensities are displayed in units of 2.00×10^{-4} cps/pixel ($0.0214 \mu\text{Jy}/\text{pixel}$).

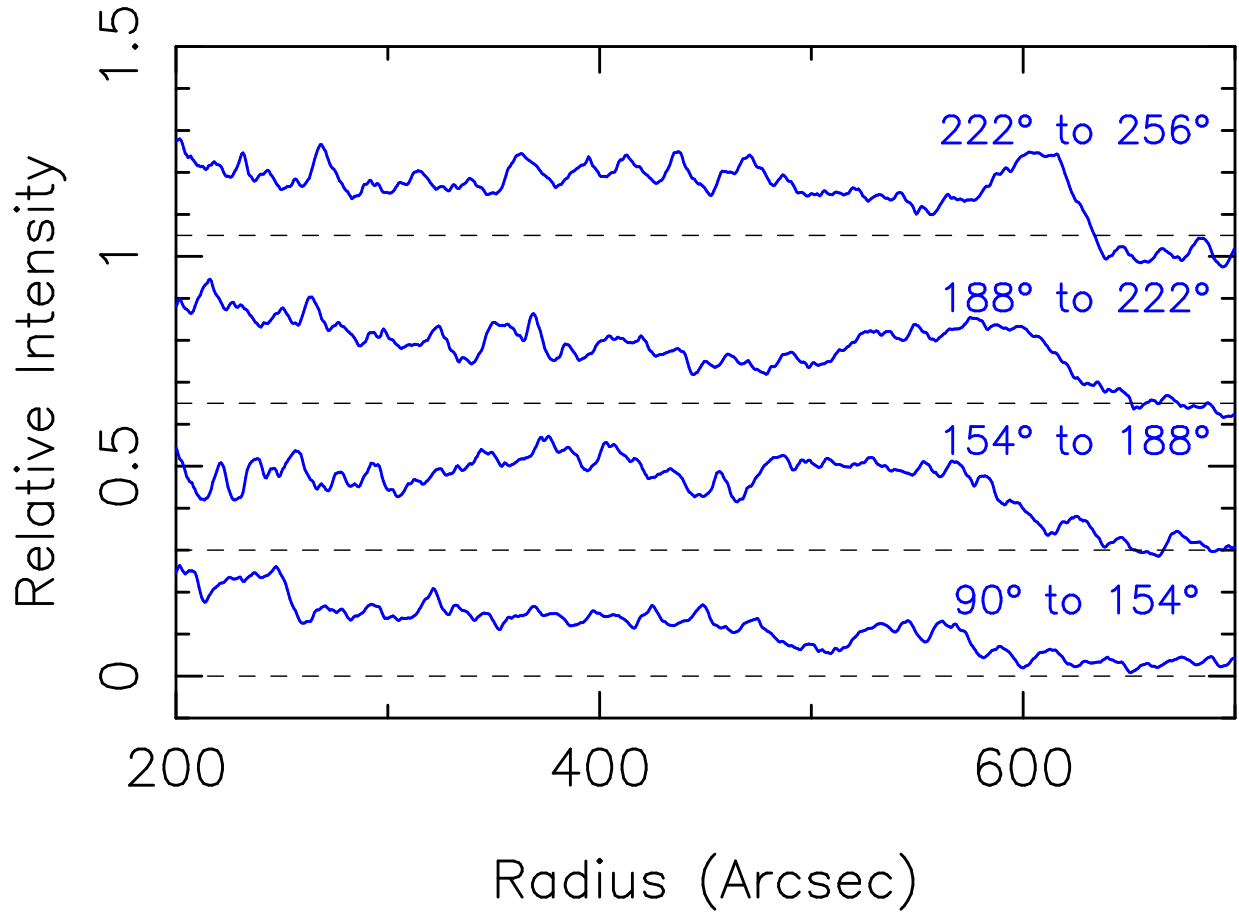


Fig. 4.— As in Fig. 3, but for angular wedges spanning the southern ring seen in the FUV emission nebula around CIT 6.

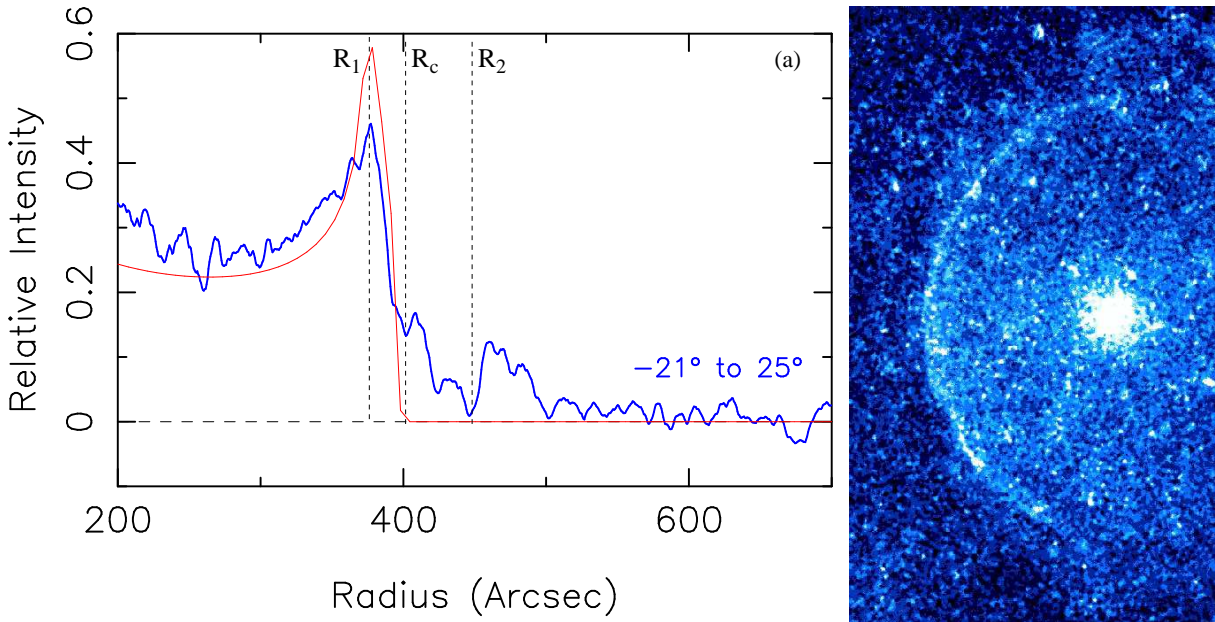


Fig. 5.— (a) Cut of radial intensity (blue) averaged over a 46° degree wedge centered at 2° in the FUV. A model fit to the intensity is shown in red, along with the approximate locations of the termination shock (R_1) and the astropause (R_c). FUV intensity units are as in Fig. 3. (b) Detail of the FUV emission, rotated from its original orientation (as in Fig 1). Box size is $10.25' \times 17.5'$; smoothing, stretch, and units as in Fig 1.